

## Large Eddy Simulation of transitional flows in rotor/stator cavity

E. TULISZKA-SZNITKO, A. ZIELINSKI, W. MAJCHROWSKI

*Institute of Thermal Engineering  
Poznan University of Technology  
Piotrowo 3, 60-965, Poznań, Poland  
e-mails: [tulizka-sznitko@put.poznan.pl](mailto:tulizka-sznitko@put.poznan.pl)  
[a.zielinski@onet.eu](mailto:a.zielinski@onet.eu)  
[wmboczek@op.pl](mailto:wmboczek@op.pl)*

AN ALGORITHM FOR the Large Eddy Simulation, with subgrid modelling based on the spectral Chebyshev–Fourier approximation, is developed for the investigation of 3D turbulent and transitional non-isothermal flows within a rotor/stator cavity. In LES we use a version of the dynamic Smagorinsky eddy viscosity model in which the Smagorinsky coefficient at a given position  $x$  depends on the history of the flow along the fluid particle pathline. Computations are based on the efficient pseudo-spectral Chebyshev–Fourier method (S. HUGUES, A. RANDRIAMAMPINANINA, *An improved projection scheme applied to pseudospectral methods for the incompressible Navier–Stokes equations*, Int. J. Numer. Methods Fluids, **28**, 501, 1998). To demonstrate the effectiveness of the proposed algorithm, computations were performed for the cavity of aspect ratio  $L = 5$  and results were compared favorably with the experimental data taken from literature.

**Key words:** spectral approximation, LES, subgrid modelling, DNS, rotating cavity flow.

Copyright © 2009 by IPPT PAN

### 1. Introduction

THE INSTABILITY STRUCTURES of the flow in the rotor/stator and rotor/rotor cavity were investigated since the sixties of the last century, mostly in reference to applications in turbomachinery. Additionally, the flow between rotating disks is one of the simplest 3D flows, highly suitable for investigating the effect of mean flow parameters on the turbulence and transitional structures [1, 4–10]. The non-isothermal flow conditions were also considered [2, 3, 11–14] showing that the thermal effects and the rotation-induced buoyancy, influence the stability characteristics and the critical conditions.

DAILY and NECE [15] investigated experimentally the flow in sealed rotor/stator cavity and identified four regimes depending on the combination of the

---

<sup>\*)</sup>The paper was presented at XVIII Polish Conference of Fluid Mechanics (KKMP), Jastrzębia Góra, 21–25 September, 2008.

rotational Reynolds number  $Re = \Omega^* R_1^{*2} / \nu^*$  and the aspect ratio  $L = (R_1^*) / 2h^*$ , where  $R_1^*$  is the radius of the outer cylinder,  $2h^*$  is the axial distance between disks and  $\Omega^*$  is the rotational speed of rotor. Two comprehensive books on the flows over a single rotating disk and on the flows through open and confined rotor/stator cavities, were published by OWEN and ROGERS [16, 17]. The transitional flows around rotating geometries were studied experimentally by SCHOUVEILER *et al.* [18], GAUTHIER *et al.* [19], MOISY *et al.* [20] and PONCET *et al.* [21]. The turbulent flows around the single rotating disk or inside the rotating cavity were investigated experimentally, among others, by DAILY and NECE [15], CHEAH *et al.* [22], SÉVERAC *et al.* [5] and ITOH *et al.* [23, 24]. SÉVERAC *et al.* [5] performed experimental investigations of the flow in an enclosed rotor/stator cavity of aspect ratio  $L = 5$  and curvature parameter  $Rm = 1.8$ , using the LDV technique. Their paper provided detailed information on the mean flows as well as on the turbulence statistics. SÉVERAC *et al.* [5] compared experimental results with the numerical results obtained using the Spectral Vanishing Viscosity method (SVV).

The transitional flows in the rotor/stator and rotor/rotor cavity were investigated using the DNS method by many authors: LOPEZ *et al.* [25], MOISY *et al.* [20], SERRE *et al.* [4, 26, 27], HEALEY [28], RASPO *et al.* [3], RANDRIAMAMPIANINA *et al.* [29, 30], TULISZKA-SZNITKO *et al.* [31–33], CRESPO *et al.* [34] and CZARNY *et al.* [35]. Numerical computations are particularly challenging for the cases with turbulent flow. The basic numerical difficulty in the rotor/stator computations for higher  $Re$  comes from the fact that in the cavity simultaneously exist areas of laminar, transitional and turbulent flows, completely different in terms of flow properties. LYGREN and ANDERSON [36] performed computations up to  $Re = 400000$  using the Direct Numerical Simulation (DNS) method and provided detailed information about coherent structures in the near-disk areas. There were some attempts to use the RANS method (ELÉNA and SCHIESTEL [14], JACQUES *et al.* [37]) to investigate the turbulent rotor/stator flows, however, modelling of these flows is very difficult due to the already mentioned flow variety. Potentially, Large Eddy Simulation (LES) can give access to large-scale vortex dynamics, provided that the physical modelling of the unresolved small-scales and the numerical approach used for the resolved scales are sufficiently accurate. The first LES computations of the flow around single rotating disk were performed by WU and SQUIRES [38]. ANDERSON and LYGREN [39], LYGREN and ANDERSON [40] performed LES of the flow in the open rotor/stator cavity using three different models and compared the results with those obtained by DNS. SÉVERAC *et al.* [5], SÉVERAC and SERRE [1] performed numerical computations for the enclosed cavity up to  $Re = 1000000$  ( $L = 5$ ,  $Rm = 1.8$ ) using the SVV method and compared the results with their LDV experimental data. The SVV technique, developed among others by

PASQUETTI [42], turned out to be a very effective numerical tool, which allows for stable discretization without sacrificing the accuracy of the spectral approximation.

In the paper, we investigate the flow in the rotor/stator cavity of the aspect ratio  $L = 5$  and curvature parameter  $Rm = 1.8$  and  $3$ , using LES based on the subgrid turbulence modelling and on the spectral Chebyshev–Fourier approximation. The cavities ( $L = 5, Rm = 1.8$ ) and ( $L = 5, Rm = 3$ ) were chosen as the flow test cases to verify the proposed SGM LES algorithm. This LES algorithm is based on a version of the dynamic Smagorinsky eddy viscosity model proposed by MENEVEAU [41], in which the averaging is performed over the fluid particle pathline. In this approach, the Smagorinsky coefficient at a given position  $\mathbf{x}$  depends on the history of the flow. The comparison of our results with the experimental data and SVV data (SÉVERAC *et al.* [5]) shows a good agreement.

In Section 2 the mathematical and geometrical models are presented. The SGM algorithm is described in Section 3. Implementation of SGM and the numerical details are shown in Section 4 and 5. In Sections 6 and 7 the mean flow and turbulence statistics are discussed respectively. Conclusions are given in Section 8.

## 2. Mathematical and numerical approach

### 2.1. Mathematical modelling

We investigate the non-isothermal flows in the cavity between stationary and rotating disks of the inner and outer radii  $R_0^*$  and  $R_1^*$ , respectively. The outer cylinder is attached to the stator and the inner one is attached to the rotor, Fig. 1. The interdisk spacing is denoted by  $2h^*$ . The rotor rotates at uniform

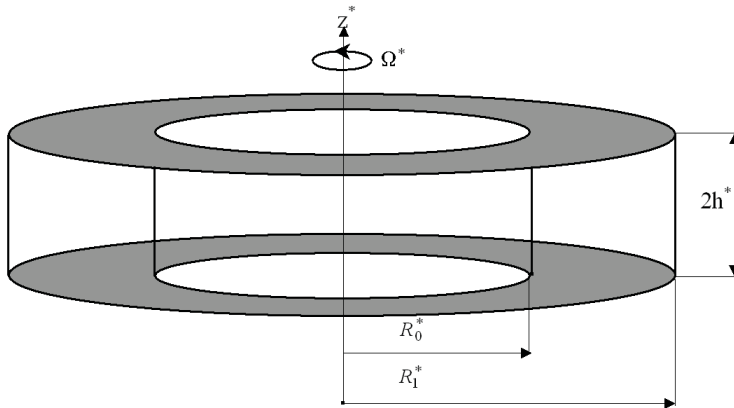


FIG. 1. Schematic picture of rotating cavity.

angular velocity  $\Omega^* = \Omega^* e_z$ ,  $e_z$  being the unit vector on the axis. The flow is described by the following Navier–Stokes, continuity and energy equations, written in a cylindrical coordinate system  $(r^*, \varphi, z^*)$  with respect to a rotating frame of reference (asterisk denotes a dimensional value):

$$(2.1) \quad \begin{aligned} \rho^* \frac{\partial \mathbf{V}^*}{\partial t^*} + \rho^* (\mathbf{V}^* \cdot \nabla) \mathbf{V}^* + \rho^* \Omega^* \times (\Omega^* \times r^*) + 2\rho^* \Omega^* \times \mathbf{V}^* \\ = -\nabla P^* + \mu^* \Delta \mathbf{V}^*, \\ \nabla \cdot \mathbf{V}^* = 0, \\ \frac{\partial T^*}{\partial t^*} + (\mathbf{V}^* \cdot \nabla) T^* = a^* \Delta T^*, \end{aligned}$$

where  $t^*$  is time,  $r^*$  is radius,  $P^*$  is pressure,  $\rho^*$  is density,  $\mathbf{V}^*$  is the velocity vector of the components in radial, azimuthal and axial directions  $(u^*, v^*, w^*)$ ,  $a^*$  is the thermal diffusivity,  $\rho^*$  is the density and  $\mu^*$  is the dynamic viscosity. To take into account the buoyancy effects induced by the involved body forces, the Boussinesq approximation is used, i.e. the density associated with the terms of centrifugal and Coriolis forces due to the disk rotation and the curvilinear motion of fluids, are all considered to be variable

$$(2.2) \quad \rho^* = \rho_r^* [1 - \beta^* (T^* - T_1^*)],$$

where  $\beta^* = -1/\rho_r^* (\partial \rho^* / \partial T^*)_p$ . The gravity force is neglected, for its magnitude is small in comparison with the centrifugal force.

The no-slip boundary conditions are applied to all rigid walls,  $u^* = w^* = 0$ . For the azimuthal velocity component, the boundary conditions are as follows:  $v^* = 0$  on the rotating disk and inner cylinder, and  $v^* = -r^* \Omega^*$  on the stator and outer cylinder. The Dirichlet boundary conditions for temperature are applied (the stator and the outer cylinder are heated). The Eqs. (2.1) are completed by the initial conditions for velocity and temperature:  $V^* = V^{*0}$  (with  $\nabla \cdot V^{*0} = 0$ ) and  $T^* = T^{*0}$  in the whole domain.

The time, length and velocity are normalized as follows:  $(\Omega^*)^{-1}$ ,  $h^*$  and  $\Omega^* R_1^*$ . The dimensionless time is denoted by  $t = t^* \Omega^*$ . The dimensionless temperature is defined in the following manner:  $\Theta = (T^* - T_1^*) / (T_2^* - T_1^*)$ , where  $T_1^*$  is temperature of the rotor and inner cylinder, and  $T_2^*$  is temperature of the stator and outer cylinder. For the non-isothermal conditions, the thermal Rossby number was introduced,  $B = \beta^* (T_2^* - T_1^*)$ . The dimensionless axial and radial coordinates are:  $z = z^* / h^*$ ;  $z \in [-1, 1]$ ,  $r = (2r^* - (R_1^* + R_0^*)) / (R_1^* - R_0^*)$ ;  $r \in [-1, 1]$ . The dimensionless components of the velocity vector in radial, azimuthal and axial directions are denoted by  $u$ ,  $v$ ,  $w$ , and dimensionless pressure is denoted by  $p$ .

## 2.2. Projection scheme for time discretization and space approximation

The temporal approximation adopted in the paper is a projection scheme, based on backward differentiation in time. The numerical code prepared in the present research for LES of the non-isothermal flow in the annular cavity, is an extended version of the DNS code developed in prof. P. Bontoux group (VANDEL *et al.* [45], RANDRIAMAMPINANINA *et al.* [29], RASPO *et al.* [3], SERRE and PULICANI [4]). In the algorithm, at each time step a pressure predictor is computed by solving the pressure Poisson equation with the pressure Neumann boundary condition.

The Navier–Stokes, continuity and energy equations (2.1) are approximated in time using a second-order semi-implicit scheme, which combines an implicit treatment of the diffusive term and an explicit Adams–Bashforth extrapolation for the non-linear convective terms.

The numerical solution is based on a pseudo-spectral collocation Chebyshev–Fourier–Galerkin approximation. In the non-homogeneous radial and azimuthal directions, Chebyshev polynomials are used with the Gauss-Lobatto distributions of the collocation points ( $r_i = \cos(\pi i/N)$  for  $0 \leq i \leq N$ ,  $z_i = \cos(\pi i/M)$  for  $0 \leq i \leq M$ ), to ensure high accuracy of the solution inside the very narrow boundary layers at the disks. The uniform mesh has been used in the statistically homogeneous azimuthal direction. The approximation of the flow variables  $\Psi = (u, w, v, p, \Theta)$  is given by a development in truncated series (SERRE and PULICANI [4]):

$$(2.3) \quad \Psi_{NMK}(r, z, \varphi, t) = \sum_{p=-K/2}^{K/2-1} \sum_{n=0}^N \sum_{m=0}^M \hat{\Psi}_{nmp}(t) T_n(r) T_m(z) e^{ip\varphi},$$

$$-1 \leq r, z \leq 1; \quad 0 \leq \varphi \leq 2\pi,$$

where  $T_n(r)$  and  $T_m(z)$  are the Chebyshev polynomials of degrees  $n$  and  $m$ , respectively, and  $N$ ,  $K$  and  $M$  are the numbers of collocation points in the radial, azimuthal and axial directions.

## 3. Incorporation of the SGM model into governing equations

In Large Eddy Simulation, each variable of the flow  $f$  is split into a large-scale anisotropic component indicated by overbar ( $\bar{f}$ ), which is computed, and a small-scale component  $f'$ , called subgrid scale, which are more isotropic and more universal and have to be modelled. This separation is obtained by applying a filter operation to the Navier–Stokes, continuity and energy equations. In the present work, Gaussian filter with a filter width equal to the grid spacing in the

azimuthal direction has been applied to the governing equations. After the filter operation, we obtain the filtered equations of motion:

$$(3.1)_1 \quad \frac{1}{L} \frac{\partial \bar{u}}{\partial r} + \frac{\bar{u}}{L(Rm+r)} + \frac{1}{L(Rm+r)} \frac{\partial \bar{v}}{\partial \varphi} + \frac{\partial \bar{w}}{\partial z} = 0,$$

$$(3.1)_2 \quad \begin{aligned} & \frac{\partial \bar{u}}{\partial t} + L(Rm+1)A(\bar{u}) \\ &= -(Rm+1) \frac{\partial \bar{p}}{\partial r} + \frac{L^2(Rm+1)^2}{\text{Re}} \left[ \Delta \bar{u} - \frac{\bar{u}}{L^2(Rm+r)^2} - \frac{2}{L^2(Rm+r)^2} \frac{\partial \bar{v}}{\partial \varphi} \right] \\ & \quad + L(Rm+1)A^{SGS}(\bar{u}), \end{aligned}$$

$$(3.1)_3 \quad \begin{aligned} & \frac{\partial \bar{v}}{\partial t} + L(Rm+1)A(\bar{v}) \\ &= -\frac{(Rm+1)}{(Rm+r)} \frac{\partial \bar{p}}{\partial \varphi} + \frac{L^2(Rm+1)^2}{\text{Re}} \left[ \Delta \bar{v} - \frac{\bar{v}}{L^2(Rm+r)^2} + \frac{2}{L^2(Rm+r)^2} \frac{\partial \bar{u}}{\partial \varphi} \right] \\ & \quad + L(Rm+1)A^{SGS}(\bar{v}), \end{aligned}$$

$$(3.1)_4 \quad \begin{aligned} & \frac{\partial \bar{w}}{\partial t} + L(Rm+1)A(\bar{w}) \\ &= -L(Rm+1) \frac{\partial \bar{p}}{\partial z} + \frac{L^2(Rm+1)^2}{\text{Re}} [\Delta \bar{w}] + L(Rm+1)A^{SGS}(\bar{w}), \end{aligned}$$

$$(3.1)_5 \quad \frac{\partial \bar{\Theta}}{\partial t} + L(Rm+1)A(\bar{\Theta}) = \frac{L^2(Rm+1)^2}{\text{Pr Re}} [\Delta \bar{\Theta}] + L(Rm+1)A^{SGS}(\bar{\Theta}),$$

where

$$(3.2)_1 \quad A(\bar{V}) = [A(\bar{u}), A(\bar{v}), A(\bar{w})]^T,$$

$$(3.2)_2 \quad \begin{aligned} A(\bar{u}) &= \frac{1}{L} \bar{u} \frac{\partial \bar{u}}{\partial r} + \frac{1}{L(Rm+r)} \bar{v} \frac{\partial \bar{u}}{\partial \varphi} + \bar{w} \frac{\partial \bar{u}}{\partial z} \\ & \quad - (1 - B\bar{\Theta}) \cdot \left( \frac{\bar{v}^2}{L(Rm+r)} + \frac{2\bar{v}}{L(Rm+1)} + \frac{(Rm+r)}{L(Rm+1)^2} \right), \end{aligned}$$

$$(3.2)_3 \quad \begin{aligned} A(\bar{v}) &= \frac{1}{L} \bar{u} \frac{\partial \bar{v}}{\partial r} + \frac{1}{L(Rm+r)} \bar{v} \frac{\partial \bar{v}}{\partial \varphi} + \bar{w} \frac{\partial \bar{v}}{\partial z} \\ & \quad + (1 - B\bar{\Theta}) \cdot \left( \frac{\bar{u}\bar{v}}{L(Rm+r)} + \frac{2\bar{u}}{L(Rm+1)} \right), \end{aligned}$$

$$(3.2)_4 \quad A(\bar{w}) = \frac{1}{L} \bar{u} \frac{\partial \bar{w}}{\partial r} + \frac{1}{L(Rm+r)} \bar{v} \frac{\partial \bar{w}}{\partial \varphi} + \bar{w} \frac{\partial \bar{w}}{\partial z},$$

$$(3.3) \quad A(\bar{\Theta}) = \frac{1}{L} \bar{u} \frac{\partial \bar{\Theta}}{\partial r} + \frac{1}{L(Rm+r)} \bar{v} \frac{\partial \bar{\Theta}}{\partial \varphi} + \bar{w} \frac{\partial \bar{\Theta}}{\partial z},$$

$$(3.4)_1 \quad A^{SGS}(\bar{u}) = - \left[ \frac{1}{L} \frac{\partial(\overline{u'u'} - \bar{u}'\bar{u}')}{\partial r} + \frac{1}{L(Rm+r)} \frac{\partial(\overline{v'u'} - \bar{v}'\bar{u}')}{\partial \varphi} \right. \\ \left. + \frac{\partial(\overline{w'u'} - \bar{w}'\bar{u}')}{\partial z} - (1 - B\bar{\Theta}) \cdot \frac{\overline{v'v'} - \bar{v}'\bar{v}'}{L(Rm+r)} \right],$$

$$(3.4)_2 \quad A^{SGS}(\bar{v}) = - \left[ \frac{1}{L} \frac{\partial(\overline{u'v'} - \bar{u}'\bar{v}')}{\partial r} + \frac{1}{L(Rm+r)} \frac{\partial(\overline{v'v'} - \bar{v}'\bar{v}')}{\partial \varphi} \right. \\ \left. + \frac{\partial(\overline{w'v'} - \bar{w}'\bar{v}')}{\partial z} + (1 - B\bar{\Theta}) \cdot \frac{\overline{u'v'} - \bar{u}'\bar{v}'}{L(Rm+r)} \right],$$

$$(3.4)_3 \quad A^{SGS}(\bar{w}) = - \left[ \frac{1}{L} \frac{\partial(\overline{u'w'} - \bar{u}'\bar{w}')}{\partial r} + \frac{1}{L(Rm+r)} \frac{\partial(\overline{v'w'} - \bar{v}'\bar{w}')}{\partial \varphi} \right. \\ \left. + \frac{\partial(\overline{w'w'} - \bar{w}'\bar{w}')}{\partial z} \right],$$

$$(3.5) \quad A^{SGS}(\bar{\Theta}) = - \left[ \frac{1}{L} \frac{\partial(\overline{u'\Theta'} - \bar{u}'\bar{\Theta}')}{\partial r} + \frac{1}{L(Rm+r)} \frac{\partial(\overline{v'\Theta'} - \bar{v}'\bar{\Theta}')}{\partial \varphi} \right. \\ \left. + \frac{\partial(\overline{w'\Theta'} - \bar{w}'\bar{\Theta}')}{\partial z} \right],$$

$$(3.6) \quad \Delta = \frac{\partial^2}{L^2 \partial r^2} + \frac{1}{L^2(Rm+r)} \frac{\partial}{\partial r} + \frac{1}{L^2(Rm+r)^2} \frac{\partial^2}{\partial \varphi^2} + \frac{\partial^2}{\partial z^2}.$$

We introduce additional notations:

$$(3.7) \quad F(\bar{V}) = [F(\bar{u}), F(\bar{v}), F(\bar{w})]^T$$

where

$$(3.8) \quad F(\bar{u}) = \Delta \bar{u} - \frac{1}{L^2(Rm+r)^2} \left( \bar{u} + 2 \frac{\partial \bar{v}}{\partial \varphi} \right), \\ F(\bar{v}) = \Delta \bar{v} - \frac{1}{L^2(Rm+r)^2} \left( \bar{v} - 2 \frac{\partial \bar{u}}{\partial \varphi} \right), \\ F(\bar{w}) = \Delta \bar{w}.$$

In the Smagorisky dynamic model, the subgrid scale, the stresses  $\sigma_{ij} = \overline{u'_i u'_j} - \bar{u}'_i \bar{u}'_j$  and energy flux  $\alpha_i = \overline{u'_i \Theta'}$  are connected with the eddy

viscosity by the following expression:

$$(3.9)_1 \quad \sigma_{ij} = -2\nu_{SGS}\bar{S}_{ij}, \quad \alpha_j = \frac{\nu_{SGS}}{\text{Pr}_{SGS}} \frac{\partial \zeta^k}{\partial x_j} \frac{\partial \bar{\Theta}}{\partial \zeta^k},$$

where

$$(3.9)_2 \quad \nu_{SGS} = C_S^2 \Delta^2 \sqrt{2\bar{S}_{ij}\bar{S}_{ij}}, \quad \bar{S}_{ij} = \frac{1}{2} \left( \frac{\partial \zeta^k}{\partial x_j} \frac{\partial \bar{u}_i}{\partial \zeta^k} + \frac{\partial \zeta^k}{\partial x_i} \frac{\partial \bar{u}_j}{\partial \zeta^k} \right).$$

In the above equations  $(x_1, x_2, x_3) = (x, y, z)$  and  $(\zeta^1, \zeta^2, \zeta^3) = (r, \varphi, z)$ . In modelling of the energy flux  $\alpha_j$ , we introduced the turbulent Prandtl number [43] denoted by  $\text{Pr}_{SGS}$ , whose definition will be given in further part of this section. In order to compute the dynamic Smagorinsky coefficient  $C_S^2$ , the filter operation is repeated with a filter width  $\hat{\Delta} = 2\Delta$ ; this filter operation is denoted by a hat. The foundation of the dynamic model is the GERMANO identity [44]:

$$(3.10)_1 \quad L_{ij} = T_{ij} - \hat{\sigma}_{ij},$$

where

$$(3.10)_2 \quad L_{ij} = \widehat{\hat{u}'_i \hat{u}'_j} - \hat{u}'_i \hat{u}'_j, \quad T_{ij} = \widehat{u'_i u'_j} - \hat{u}'_i \hat{u}'_j, \quad \hat{\sigma}_{ij} = \widehat{u'_i u'_j} - \widehat{\hat{u}'_i \hat{u}'_j},$$

which relates subgrid-scale stresses computed at two different filter widths:  $\Delta(\sigma_{ij})$  and  $\hat{\Delta}(T_{ij})$ . Finally, the dynamic constant (if  $C_S^2$  is constrained to have no variation over homogeneous direction) is calculated from the expression:

$$(3.11)_1 \quad C_S^2 = \frac{\langle L_{mn} M_{mn} \rangle}{\langle M_{pq} M_{pq} \rangle},$$

where

$$(3.11)_2 \quad M_{ij} = 2\Delta^2 \left[ \widehat{|\bar{S}| \bar{S}_{ij}} - 4\widehat{|\hat{S}| \hat{S}_{ij}} \right]$$

and  $\langle \rangle$  denotes averaging over the homogeneous direction. The resulting coefficient field in the Smagorinsky dynamic model is highly variable and contains a large percentage of negative values, what leads to numerical instability. In most applications, the model is stabilized by averaging over the direction of statistical homogeneity. The dynamic Smagorinsky model was tested in the present paper with averaging performed over the azimuthal direction (the only homogeneous direction in the rotating cavity). However, due to difficulties with the numerical stability this model was rejected. To overcome this problem we have used the version of the dynamic Smagorinsky model proposed by MENEVEAU *et al.* [41]. Meneveau *et al.* proposed to perform averaging rather over the fluid particle

pathline, instead of averaging over the direction of statistical homogeneity, which makes this approach applicable for more complicated non-homogeneous flows. In this model, coefficient  $C_S^2$  is derived by minimization of the total error:

$$(3.12)_1 \quad E = \int_{-\infty}^t e_{ij}(x_1, t_1) e_{ij}(x_1, t_1) W(t-t_1) dt,$$

thought as an accumulation of the square of local error:

$$(3.12)_2 \quad e_{ij} = L_{ij}(x_1, t_1) - C_S^2(x, t) M_{ij}(x_1, t_1)$$

over the trajectory of the fluid particle. In Eqs. (3.12)  $x$  is the position of the particle at the considered time  $t$ ,  $x_1$  is the position of particle at the previous time section  $t_1$ ,  $W(t-t_1)$  is the weighting function which controls the importance of events in different time sections. After minimization of error ( $\partial E / \partial (C_S^2) = 0$ ), we obtain the value of the dynamic Smagorinsky coefficient [41]:

$$(3.13) \quad C_S^2 = \frac{L_{LM}}{L_{MM}} = \frac{\int_{-\infty}^t L_{ij}(x_1, t_1) M_{ij}(x_1, t_1) W(t-t_1) dt}{\int_{-\infty}^t M_{ij}(x_1, t_1) M_{ij}(x_1, t_1) W(t-t_1) dt}.$$

We use exponential weighting function of the form  $W(t-t_1) = \tau^{-1} e^{-(t-t_1)/\tau}$ , for which we can obtain  $L_{LM}$  and  $L_{MM}$  from the following equations [41]:

$$(3.14) \quad \begin{aligned} \frac{DL_{LM}}{dt} &= \frac{1}{\tau} (L_{ij} M_{ij} - L_{LM}), \\ \frac{DL_{MM}}{dt} &= \frac{1}{\tau} (M_{ij} M_{ij} - L_{MM}). \end{aligned}$$

These equations can be solved by using simple approximation formula:

$$(3.15) \quad \frac{L_{LM}^{n+1}(x) - L_{LM}^n(x - \bar{u}^n)}{\Delta t} = \frac{1}{\tau} [(L_{ij}(x) M_{ij}(x))^{n+1} - L_{LM}^{n+1}(x)],$$

where  $(x - \bar{u}^n)$  is the location of the particle in the previous time section  $t_1$  and value  $L_{LM}^n$  at this point must be found by interpolation. In Eqs. (3.14)  $\tau$  is the time scale over which averaging is performed. In the present paper we performed computations for  $\tau = a\Delta (M_{ij} L_{ij})^{-1/4}$  (we chose the time scale proportional to the filter width  $\Delta$  because averaging over the time scale of the smallest resolved turbulent motion eliminates the unwanted numerical noise [41]). Coefficient “ $a$ ” was chosen based on the numerical experiment.

From (3.15) we obtain:

$$(3.16) \quad \begin{aligned} L_{LM}^{n+1}(x) &= H(\varepsilon (L_{ij} M_{ij})^{n+1}(x) + (1 - \varepsilon) L_{LM}^n(x - \bar{u}\Delta t)), \\ L_{MM}^{n+1}(x) &= (\varepsilon (M_{ij} M_{ij})^{n+1}(x) + (1 - \varepsilon) L_{MM}^n(x - \bar{u}\Delta t)). \end{aligned}$$

In the above equations,  $H$  is the ramp function ( $H(b) = b$  if  $b > 0$  and zero otherwise) and  $\varepsilon = \Delta t / (\tau^n (1 + \Delta t / \tau^n))$  is the weighting function. In the present paper we additionally averaged the final Smagorinsky coefficient field in the azimuthal direction.

For the energy equation we adopted LILLY'S [43] approach to the Meneveau model by introducing the turbulent Prandtl number  $\text{Pr}_{SGS}$ :

$$(3.17) \quad \frac{1}{\text{Pr}_{SGS}} = \frac{L_{PRMM}^{n+1}}{L_{RRML}^{n+1}},$$

where

$$(3.18) \quad \begin{aligned} L_{PRMM}^{n+1}(x) &= H(\varepsilon(P_j R_j M_{ij}^2)^{n+1}(x) + (1 - \varepsilon)L_{PRMM}^n(x - \bar{u}^n \Delta t)), \\ L_{RRML}^{n+1}(x) &= \varepsilon(R_j^2 M_{ij} L_{ij})^{n+1}(x) + (1 - \varepsilon)L_{RRML}^n(x - \bar{u}^n \Delta t), \end{aligned}$$

$$(3.19) \quad \begin{aligned} P_j &= \widehat{\bar{u}_j \bar{\Theta}} - \hat{u}_j \hat{\Theta}, \\ R_j &= 2\Delta^2 \left( |\widehat{\bar{S}}| \frac{\partial \bar{\Theta}}{\partial x_j} - 4|\hat{S}| \frac{\partial \hat{\Theta}}{\partial x_j} \right). \end{aligned}$$

In the present paper we computed  $\text{Pr}_{SGS}$  in every time step.

#### 4. SGM model implementation

In every time step the computations are started with the pressure predictor;  $p^p$  is computed by solving the pressure Poisson equation:

$$(4.1)_1 \quad \Delta \bar{p}^{p,n+1} = \text{div}[-2A(\bar{V})^n + A(\bar{V})^{n-1} + (2A^{SGS}(\bar{V})^n - A^{SGS}(\bar{V})^{n-1})].$$

The boundary Neumann condition is obtained by projecting Eq. (2.1)<sub>1</sub> on the vector normal (denoted by  $n$ ) to the border of domain:

$$(4.1)_2 \quad \frac{\partial \bar{p}^p}{\partial n} = \frac{L(Rm + 1)}{\text{Re}} (2F(\bar{V})^n - F(\bar{V})^{n-1}) + (2A^{SGS}(\bar{V})^n - A^{SGS}(\bar{V})^{n-1}) - (2A(\bar{V})^n - A(\bar{V})^{n-1}).$$

The predictor step is completed by solving the Helmholtz equation with the appropriate boundary conditions to obtain the velocity predictor:

$$\begin{aligned}
(4.2)_1 \quad & \left( \Delta - \frac{1}{L^2(Rm+r)^2} - \frac{1}{L^2(Rm+1)^2} \frac{3\text{Re}}{2\delta t} \right) \bar{u}^p \\
& = \frac{\text{Re}}{L^2(Rm+1)^2} \left[ \frac{-4\bar{u}^n + \bar{u}^{n+1}}{2\delta t} \right. \\
& \quad \left. + L(Rm+1) \left( 2A(\bar{u})^n - A(\bar{u})^{n-1} - (2A^{SGS}(\bar{u})^n - A^{SGS}(\bar{u})^{n-1}) + \frac{1}{L} \frac{\partial \bar{p}^p}{\partial r} \right) \right] \\
& \quad + \frac{2}{L^2(Rm+r)^2} \left( 2 \frac{\partial \bar{v}^n}{\partial \varphi} - \frac{\partial \bar{v}^{n-1}}{\partial \varphi} \right), \\
(4.2)_2 \quad & \left( \Delta - \frac{1}{L^2(Rm+r)^2} - \frac{1}{L^2(Rm+1)^2} \frac{3\text{Re}}{2\delta t} \right) \bar{v}^p \\
& = \frac{\text{Re}}{L^2(Rm+1)^2} \left[ \frac{-4\bar{v}^n + \bar{v}^{n+1}}{2\delta t} \right. \\
& \quad \left. + L(Rm+1) \left( 2A(\bar{v})^n - A(\bar{v})^{n-1} - (2A^{SGS}(\bar{v})^n - A^{SGS}(\bar{v})^{n-1}) + \frac{1}{L(Rm+r)} \frac{\partial \bar{p}^p}{\partial \varphi} \right) \right] \\
& \quad - \frac{2}{L^2(Rm+r)^2} \left( 2 \frac{\partial \bar{u}^n}{\partial \varphi} - \frac{\partial \bar{u}^{n-1}}{\partial \varphi} \right), \\
(4.2)_3 \quad & \left( \Delta - \frac{1}{L^2(Rm+1)^2} \frac{3\text{Re}}{2\delta t} \right) \bar{w}^p = \frac{\text{Re}}{L^2(Rm+1)^2} \left[ \frac{-4\bar{w}^n + \bar{w}^{n+1}}{2\delta t} \right. \\
& \quad \left. + L(Rm+1) \left( 2A(\bar{w})^n - A(\bar{w})^{n-1} - (2A^{SGS}(\bar{w})^n - A^{SGS}(\bar{w})^{n-1}) + \frac{\partial \bar{p}^p}{\partial z} \right) \right].
\end{aligned}$$

The predicted velocity field is corrected by taking into account the pressure gradient at time  $t^{n+1}$ , so that the final velocity field satisfies the incompressibility constraint

$$(4.3)_1 \quad \frac{1}{L(Rm+1)} \frac{3}{2\delta t} [\bar{V}^{n+1} - \bar{V}^p] = - [\nabla \bar{p}^{n+1} - \nabla \bar{p}^p],$$

$$(4.3)_2 \quad \nabla \cdot \bar{V}^{n+1} = 0$$

with the boundary condition:

$$(4.3)_3 \quad v^{n+1} \cdot n = v^p \cdot n.$$

Correction of the velocity field is done by computation of the new variable  $\phi = \frac{2\delta t}{3} (\bar{p}^{n+1} - \bar{p}^p)$  from the elliptic Poisson equation:

$$(4.4)_1 \quad \Delta \phi = \frac{1}{L(Rm+1)} \text{div}(\bar{V}^p)$$

with the boundary condition

$$(4.4)_2 \quad \nabla(\phi) \cdot n = 0.$$

After solving Eqs. (4.4)<sub>1</sub> and (4.4)<sub>2</sub> we obtain corrected values of three components of velocity and pressure. In the last step we compute the temperature field from the energy Helmholtz equation

$$(4.5)_1 \quad \left( \Delta - \frac{1}{L^2(Rm+1)^2} \frac{3 \text{Pr Re}}{2\delta t} \right) \bar{\Theta}^{n+1} = \frac{\text{Pr Re}}{L^2(Rm+1)^2} \left[ \frac{-4\bar{\Theta}^n + \bar{\Theta}^{n+1}}{2\delta t} \right] \\ + \frac{\text{Pr Re}}{L(Rm+1)} [(2A(\bar{\Theta})^n - A(\bar{\Theta})^{n-1} - (2A^{SGS}(\bar{\Theta})^n - A^{SGS}(\bar{\Theta})^{n-1}))]$$

with the boundary conditions:

$$(4.5)_2 \quad \bar{\Theta} = 1 \quad \text{for } z = -1, -1 \leq r \leq 1 \text{ and for } r = 1, -1 \leq z \leq 1,$$

$$(4.5)_3 \quad \bar{\Theta} = 0 \quad \text{for } z = 1, -1 \leq r < 1 \text{ and for } r = -1, -1 < z \leq 1.$$

Ultimately, the solution of the Navier–Stokes, continuity and energy equations is reduced to the solutions of uncoupled Poisson or Helmholtz equations. Each variable  $\Psi = [\bar{u}^p, \bar{v}^p, \bar{w}^p, \bar{p}^p, \bar{\Theta}, \phi]$  is the solution of a 3D equation of the form

$$(4.6) \quad [\Delta - \lambda I] \Psi = S,$$

which can be solved effectively by the diagonalization technique (SERRE and PULICANI [4]). In the SGM model the diagonalization technique is the same as in DNS: however, evaluation of the  $S$  matrix in SGM is more time-consuming. We estimate that the ratio of CPU time needed for SGM and DNS is equal to about 1.3.

## 5. Numerical details

In the paper we performed computations using DNS as long as the differences between DNS and LES were negligible; for the higher Re we switched to LES. Figure 2 shows the instability characteristics of the azimuthal velocity component obtained in the middle section of the stator boundary layer for Re = 35000 and 45000, using LES and DLS ( $L = 5$ ,  $Rm = 3$ ,  $B = 0.1$ ). Up to Reynolds number Re = 35000, the differences between DNS and LES are not visible in the instability characteristics. Differences have been observed for Re = 45000 and  $t > 20$  (Fig. 2b).

The accuracy of the mathematical description of the flow near the disks has been checked by analysing the distribution of the axial wall coordinate  $(z^+)_m =$

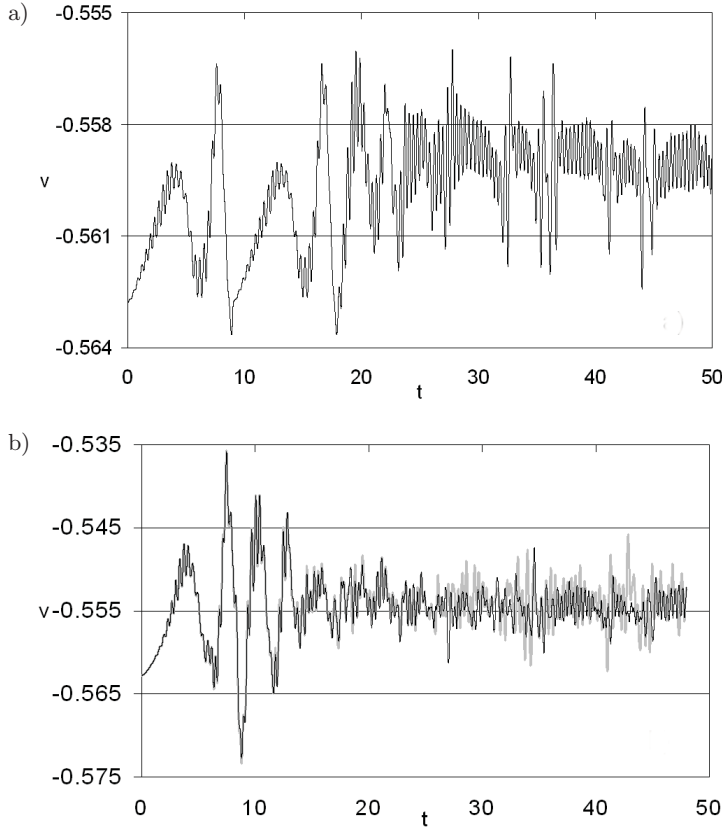


FIG. 2. Instability characteristics obtained in the middle section of the stator boundary layer,  $L = 5$ ,  $Rm = 3$ ,  $B = 0.1$ ,  $r = 0$ , a)  $Re = 35000$ , b)  $Re = 45000$ , comparison of DNS and LES.

$z_m^* v_\tau^* / \nu^*$  along the radius, where  $z_m^*$  is the smallest cell in the axial direction, and  $v_\tau^*$  is the total friction velocity  $v_\tau^* = [\nu^{*2}((\partial u^* / \partial z^*)^2 + (\partial v^* / \partial z^*)^2)]^{1/4}$ . Distributions presented in Fig. 3 were obtained for ( $L = 5$ ,  $Rm = 3$ ,  $Re = 150000$ ,  $B = 0.1$ ) and for number of collocation points in the axial directions equal 81 ( $z_m = z^* / h^* = 7.7 \cdot 10^{-4}$ ). SÉVERAC *et al.* [5] used the value  $(z^+)_m < 1$  as a criterion for precise description in the near-wall area. We can see from Fig. 3 that condition  $(z^+)_m < 1$  is satisfied even near the outer cylinder.

The spatial accuracy of the algorithm was analyzed by evaluating the maximum divergence  $(\text{div}(V))_{\max}$  in the inner domain. Results of the simulations performed for different meshes,  $(32 \times 32 \times 32)$ ;  $(48 \times 48 \times 48)$ ,  $(64 \times 64 \times 64)$  are presented in Table 1 ( $L = 5$ ,  $Rm = 3$ ,  $Re = 15000$ ,  $B = 0.1$ ). We can see that the exponential convergence property of the pseudo-spectral method is preserved in SGM. Additionally, the SGM model does not reduce the accuracy of the solution in comparison to the DNS solution, even for higher Reynolds numbers.

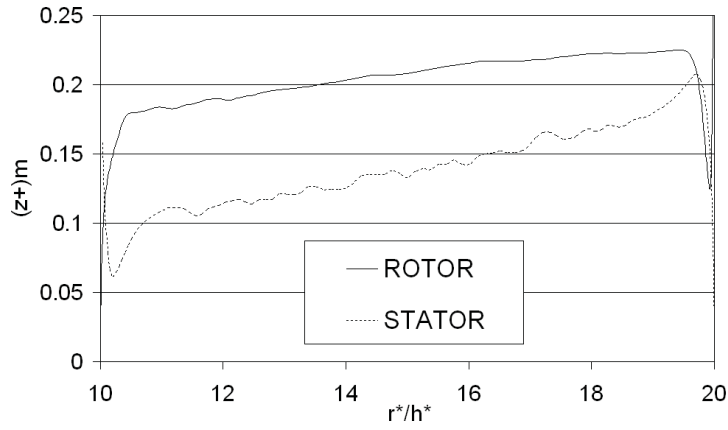


FIG. 3. Distributions of  $(z^+)_m$  along the disks obtained for  $(\text{Re} = 150000, L = 5, Rm = 3, B = 0.1)$ .

Table 1. The accuracy of the SGM method.

	$32 \times 32 \times 32$	$48 \times 8 \times 48$	$64 \times 64 \times 64$
$(\text{div}(V))_{\max}$ $L = 5, Rm = 3, \text{Re} = 150000, B = 0.1$	$2.5 \cdot 10^{-5}$	$2.9 \cdot 10^{-6}$	$1.2 \cdot 10^{-7}$

## 6. Basic flow

Let us consider the mean flow obtained for  $(L = 5, Rm = 3, B = 0.1)$  and  $(L = 5, Rm = 1.8, B = 0.0)$ , and for different Reynolds numbers. Computations were performed for the mesh  $(125 \times 125 \times 81)$  and for the time increment  $\delta t = 0.001$ .

For all the considered Reynolds numbers  $25000 \leq \text{Re} \leq 150000$  the flow exhibits typical Batchelor behaviour, i.e. the flow consists of two disjoint boundary layers on each disk and of a central inviscid core flow. The flow is pumped radially outwards along the rotor and circulates along the stator, Fig. 4.

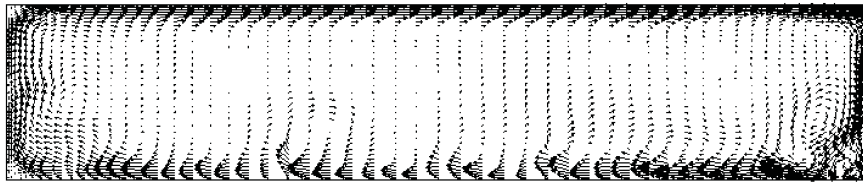


FIG. 4. Flow in the meridian section obtained for cavity  $(L = 5, Rm = 3, \text{Re} = 100000, B = 0.1)$ . SGM.

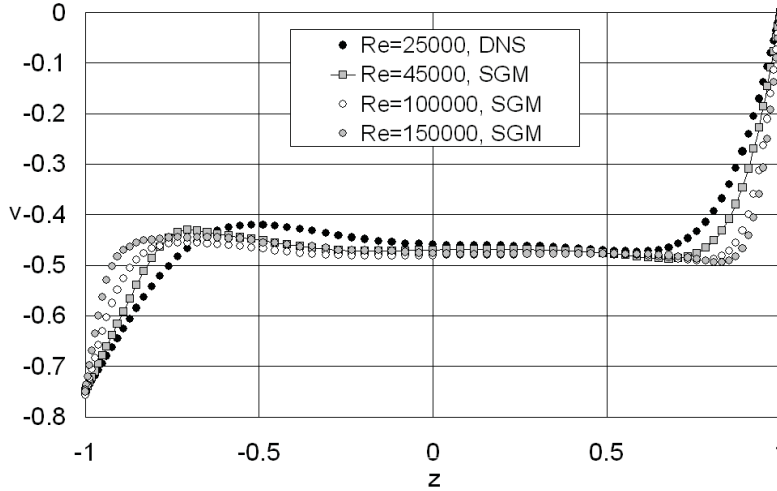


FIG. 5. Axial profiles of the azimuthal velocity component obtained in the middle section ( $r = 0$ ) of cavity ( $L = 5$ ,  $Rm = 3$ ,  $B = 0.1$ ).

Figure 5 shows the mean axial profiles of the azimuthal velocity component obtained in the middle section of cavity ( $L = 5$ ,  $Rm = 3$ ,  $B = 0.1$ ) for different Reynolds numbers. From Fig. 5 we can see that the azimuthal velocity component profiles obtained for  $Re = 25000$  and  $45000$  are laminar (S-shaped profiles), whereas profiles obtained for  $Re = 100000$  and  $150000$  are turbulent. We can see that the thickness of the rotor boundary layer decreased by factor 2 between Reynolds number  $Re = 25000$  and  $150000$ .

To verify our LES results, we performed computations for the cavity ( $L = 5$ ,  $Rm = 1.8$ ,  $B = 0$ ) and compared the results with the experimental and numerical results obtained by SÉVERAC *et al.* [5] for the same parameters (Fig. 6). In Fig. 6 we compared the azimuthal and radial velocity profiles normalized by  $\Omega^*r^*$  ( $\bar{u}_s = u(Rm + 1)/(Rm + r)$ ,  $\bar{v}_s = v(Rm + 1)/(Rm + r)$ ). From Fig. 6 we can see that agreement between the results is very good. The central inviscid core is characterized by very small radial velocity component,  $u \sim 0$ , and the almost constant azimuthal one (Figs. 5 and 6). The entrainment coefficients of the rotating fluid ( $K$ ), defined as the ratio of the tangential velocity in the core divided by the tangential velocity of the disk at the same radius, were computed and the results were compared with results obtained by SÉVERAC *et al.* [5]. For ( $L = 5$ ,  $Rm = 1.8$ ,  $Re = 100000$ ,  $B = 0.0$ ) in the middle section ( $r = 0$ ) we obtained  $K = 0.36$ , whereas SÉVERAC *et al.* [5] in the middle section for the same parameters obtained  $K = 0.35$  from both the numerical (SVV) and experimental investigations. For ( $L = 5$ ,  $Rm = 3$ ,  $Re = 100000$ ,  $B = 0.1$ ) in the middle section ( $r = 0$ ) we received  $K = 0.362$ . The differences in the value of  $K$

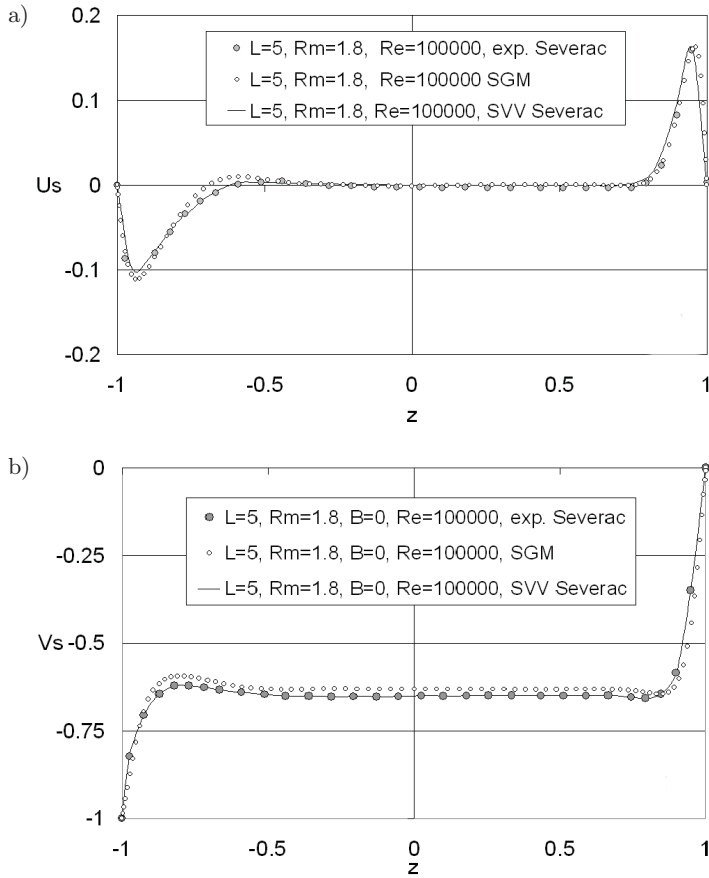


FIG. 6. Meridian velocity profiles obtained at middle section  $r = 0$  of cavity ( $L = 5$ ,  $Rm = 1.8$ ,  $B = 0$ ) by SGM (present paper), SVV and in experiment (SÉVERAC *et al.* [5]); a) radial velocity component, b) azimuthal velocity component.

obtained by using DNS and LES are negligible. Analysis of parameter  $K$  along the disk shows that  $K$  increases towards the outer end-wall.

More information about the mean flow can be obtained from polar plots of the mean radial and azimuthal velocity components. Figures 7a, b and c show the polar plots obtained in three radial sections  $r^*/h^* = 10.6, 15.0, 19.4$  of the cavity ( $L = 5$ ,  $Rm = 3$ ,  $Re = 25000, 100000, 150000$ ,  $B = 0.1$ ). The polar profiles in the rotor boundary layer obtained for considered  $Re$  are typical for the laminar flows; LES results obtained for  $Re = 100000$  and  $150000$  are very close to the DNS solution obtained for  $Re = 25000$ . In the stator boundary layer there are larger differences between the results obtained for different Reynolds numbers. The polar plot obtained for  $Re = 150000$  is more triangular, which is typical for the turbulent boundary layer (LYGREN and ANDERSON [36]). From

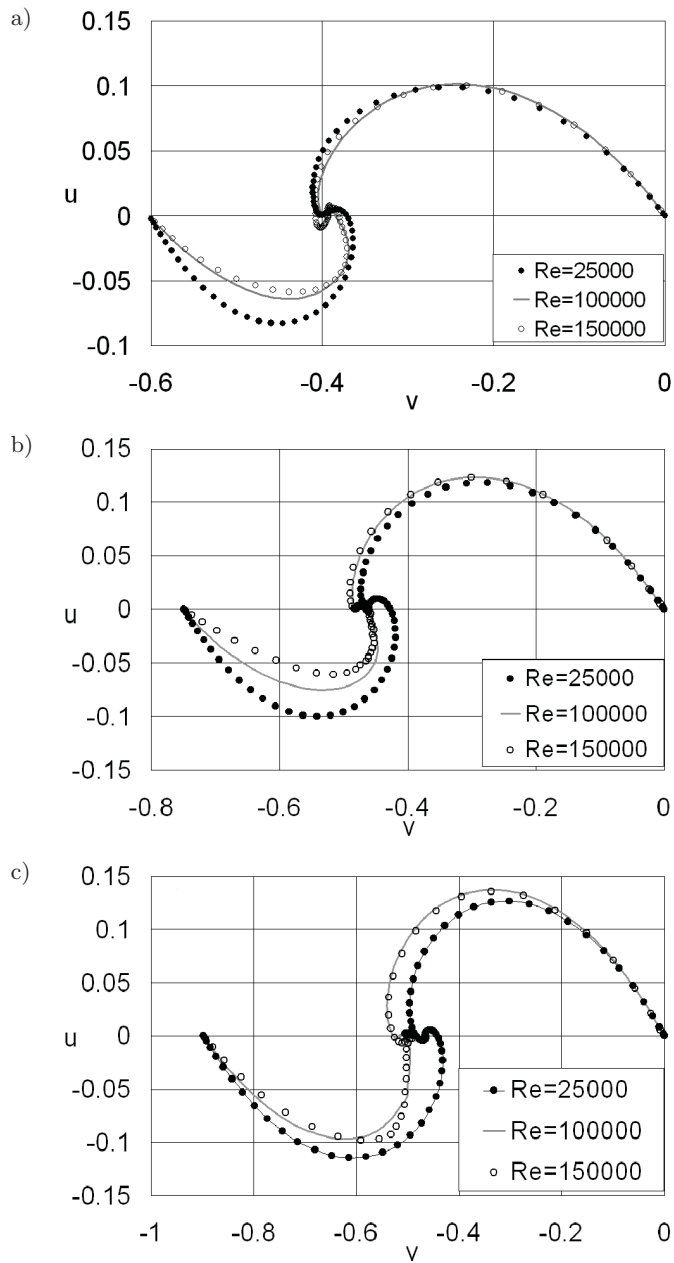


FIG. 7. Polar plots of the mean radial and azimuthal velocity components obtained in different radial sections of the cavity for different Reynolds numbers; a)  $r^*/h^* = 10.6$ , b) 15.0, c) 19.4 ( $L = 5$ ,  $Rm = 5$ ,  $B = 0.1$ ). SGM.

Fig. 7 we can see that the stator boundary layer is weakly turbulent, with the maximum turbulence at the junction between stator and outer cylinder (Fig. 7c).

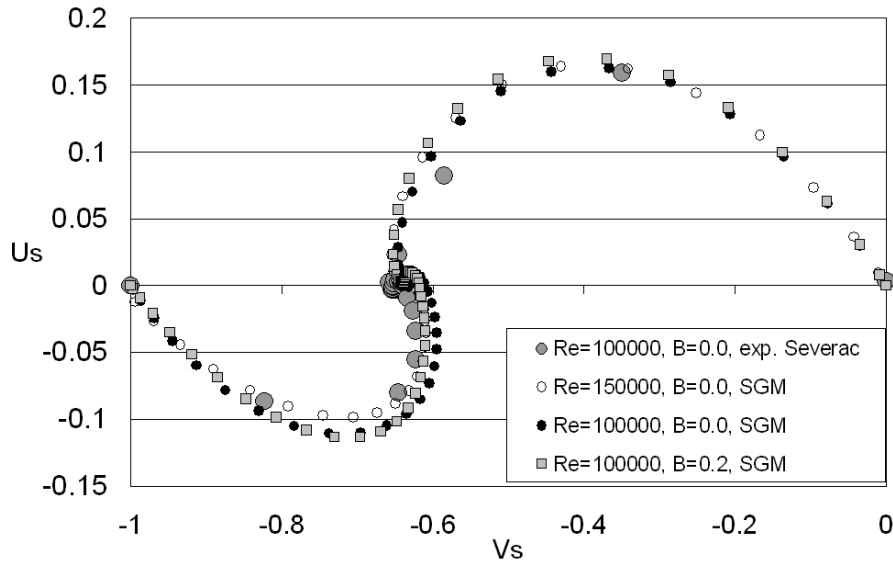


FIG. 8. Polar plots of the mean radial and azimuthal velocity components obtained in the middle section of cavity ( $L = 5$ ,  $Rm = 1.8$ ,  $B = 0$ ). Comparison between SGM (present paper) and experimental data (SÉVERAC *et al.* [5]).

To verify the SGM results, polar plots obtained in the middle section of the cavity ( $L = 5$ ,  $Rm = 1.8$ ,  $Re = 100000$ ,  $150000$ ,  $B = 0$ ) are compared to the experimental data of SÉVERAC *et al.* [5] obtained for ( $L = 5$ ,  $Rm = 1.8$ ,  $Re = 100000$ ,  $B = 0$ ), (Fig. 8). The radial and azimuthal velocity components in Fig. 8 were normalized with  $\Omega^*r^*$ . From Fig. 8 we can see that agreement between the SGM results and experimental data obtained by SÉVERAC *et al.* [5] is very good.

## 7. Turbulence field

To verify our transitional results, we compared the instability structures obtained for the Reynolds numbers close to the critical Reynolds number of transition to unsteadiness, with the experimental results of SCHOUVEILER *et al.* [18] and GAUTHIER *et al.* [19]. This detailed analysis of comparison can be found in TULISZKA-SZNITKO *et al.* [32]. In the transitional stator boundary layer, the axisymmetric propagating vortices interpreted as the type II instability and positive spiral vortices interpreted as the type I instability were observed. For higher  $Re$  structures in the stator, the boundary layers evolve from spiral

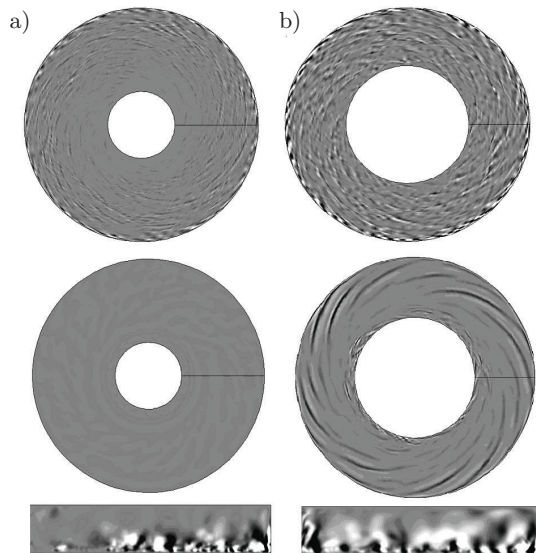


FIG. 9. Iso-lines of the disturbances of azimuthal velocity component in the azimuthal sections of the stator and rotor boundary layer and the iso-lines of the axial velocity component in the meridian section obtained for  $Re = 100000$ ; a) ( $L = 5, Rm = 1.8, B = 0.0$ ), b) ( $L = 5, Rm = 3, B = 0.1$ ). SGM.

vortices to more annular vortices. Figure 9 shows the iso-lines of the azimuthal velocity component disturbances in the azimuthal sections of the stator and rotor boundary layer, and the iso-lines of the axial velocity component in the meridian sections of the cavities ( $L = 5, Rm = 1.8, Re = 100000, B = 0$ ) and ( $L = 5, Rm = 3, Re = 100000, B = 0.1$ ). Computations have shown that the turbulence is mostly concentrated in the stator boundary layer, with a maximum at the junction between the stator and outer cylinder. It is also visible in Fig. 10, where the iso-lines of the instantaneous turbulence kinetic

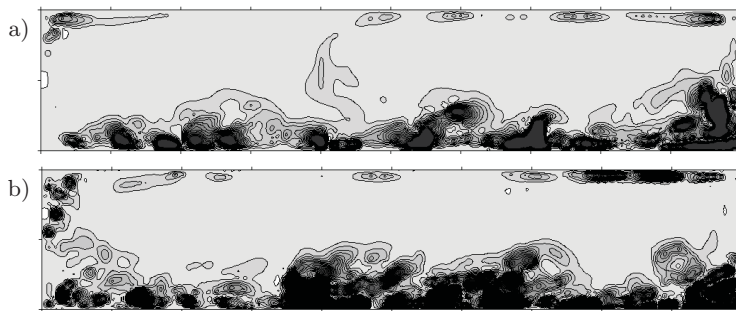


FIG. 10. The iso-lines of the instantaneous turbulence kinetic energy obtained for a)  $Re = 100000$ , b)  $Re = 150000, B = 0.1, L = 5, Rm = 3$ . SGM.

energy obtained for  $Re = 100000$  and  $150000$  ( $L = 5$ ,  $Rm = 3$ ,  $B = 0.1$ ) are displayed. From these figures we can see that the turbulence is mostly confined to the stator and the shroud areas, although weak turbulent areas are also observed on the rotating inner cylinder, where disturbances coming from the stator are transported towards the rotor.

Within the frame of this work we monitored the ratio of eddy viscosity to molecular viscosity,  $\nu_{SGS}^*/\nu^*$ . The axial profiles  $\nu_{SGS}^*/\nu^* = f(z)$  obtained for  $r = 0$  and for  $Re = 100000$ ,  $150000$  ( $L = 5$ ,  $Rm = 3$ ,  $B = 0.1$ ) are presented in Fig. 11. We can see that the subgrid viscosity is accumulated in the stator boundary layer where the turbulence is mostly confined.

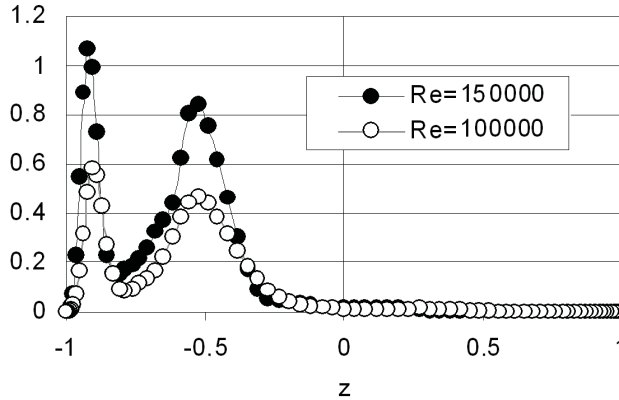


FIG. 11. Distributions of  $\nu_{SGS}^*/\nu^*$  versus  $z$ .  $Re = 100000$  and  $150000$ , ( $L = 5$ ,  $Rm = 3$ ,  $B = 0.1$ ,  $r = 0$ ). SGM.

To verify our algorithm, the axial profiles of Reynolds stress tensor components obtained by SGM in the present paper were compared with the experimental (LDV) and numerical (SVV) data of SÉVERAC *et al.* [5]. In Figs. 12a and b we analyzed the axial profiles of two main Reynolds stress tensor components  $\sqrt{v'v'}(Rm + 1)/(Rm + r)$  and  $\sqrt{u'u'}(Rm + 1)/(Rm + r)$  obtained in different radial sections of the cavity ( $L = 5$ ,  $Rm = 1.8$ ,  $Re = 100000$ ,  $B = 0.0$ ). In Figs. 13a and b the axial distributions of  $\sqrt{v'v'}(Rm + 1)/(Rm + r)$  and  $\sqrt{u'u'}(Rm + 1)/(Rm + r)$ , obtained in the middle section of the cavity are compared to the experimental and numerical results of SÉVERAC *et al.* [5]. Additionally, in Fig. 13 the results obtained for  $Re = 150000$ ,  $B = 0.0$  and  $Re = 100000$ ,  $B = 0.2$  are presented. From Fig. 13 we can see that agreement of all results is good. SGM predicts very well the radial Reynolds stress tensor components in the stator and rotor boundary layers. The values of radial Reynolds stress tensor components in the central core obtained experimentally are slightly higher than those obtained by applying the SGM and SVV meth-

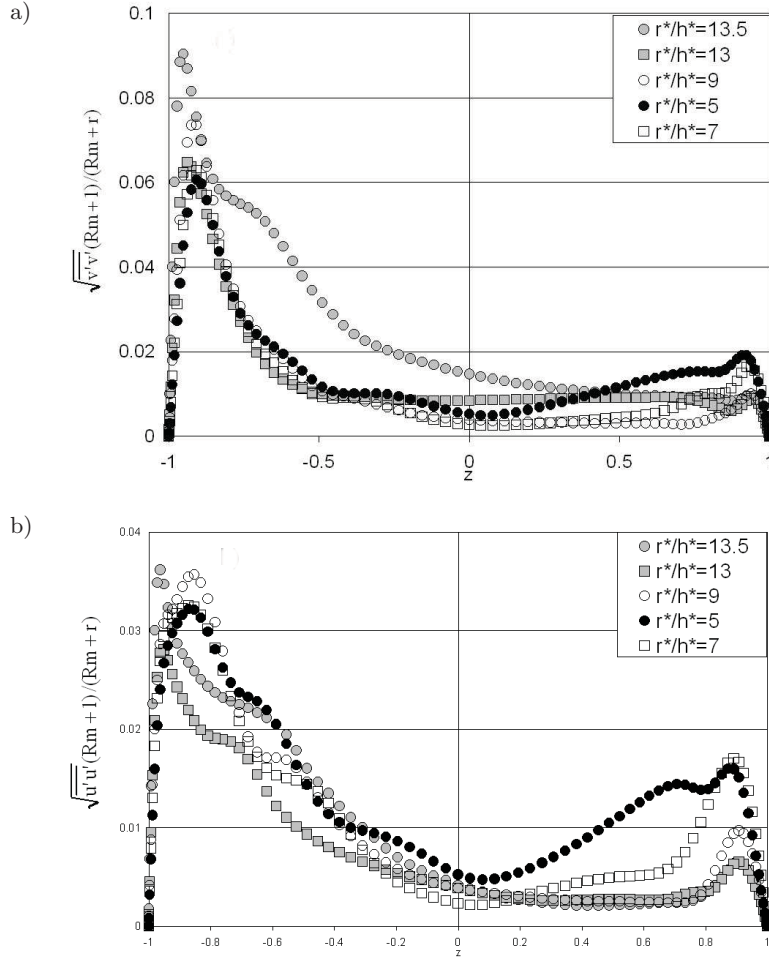


FIG. 12. Axial distributions of the Reynolds stress tensor components: a)  $\sqrt{\overline{v'v'}}(Rm+1)/(Rm+r)$ , b)  $\sqrt{\overline{u'u'}}(Rm+1)/(Rm+r)$  obtained in different sections of cavity  $L = 5$ ,  $Rm = 1.8$ ,  $B = 0.0$ ,  $Re = 100000$ . SGM.

ods. From Fig. 13 we can see that the turbulence anisotropy, resulting from our computations and also from SVV results, is larger than that resulting from experimental data of SÉVERAC *et al.* [5]. Comparison of computations obtained for  $B = 0.0$  and  $B = 0.2$  shows that with increasing  $B$  (heated stator), both the analyzed Reynolds stress tensor components increase in the central core but decrease in the vicinity of the rotor. From Figs. 12a and b we can see that the largest values of the Reynolds stress tensor components were obtained in the radial section  $r^*/h^* = 13.5$  very close to the outer end-wall, where the maximum of turbulence was observed.

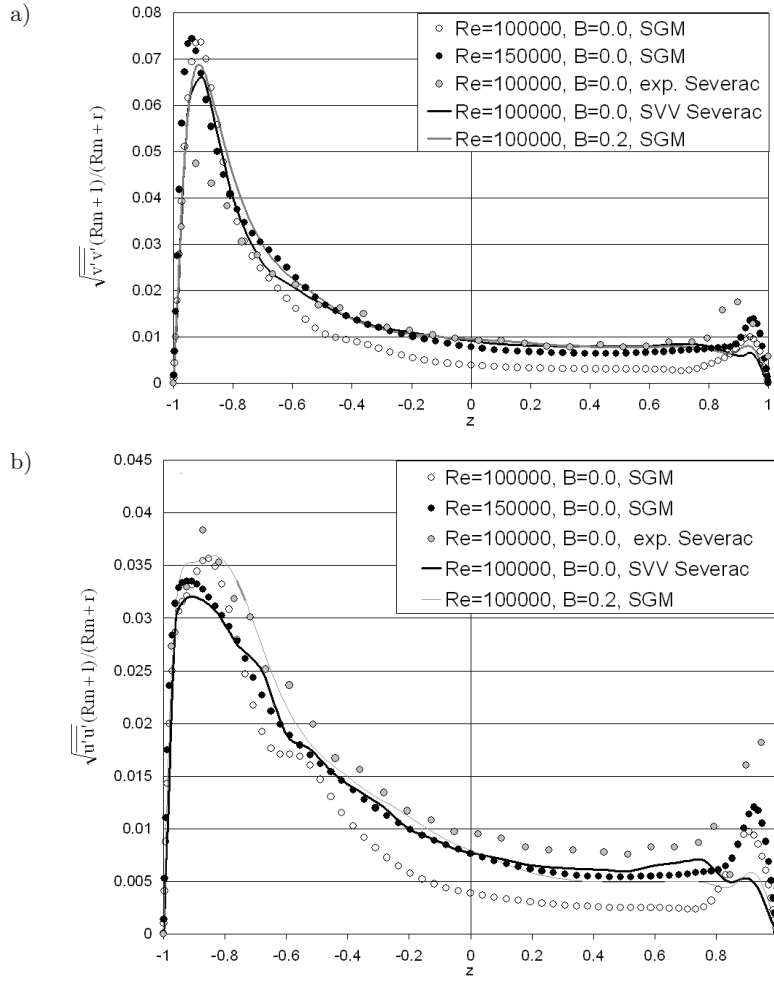


FIG. 13. Axial distributions of the Reynolds stress tensor components: a)  $\sqrt{v'v'}(Rm+1)/(Rm+r)$ , b)  $\sqrt{u'u'}(Rm+1)/(Rm+r)$  obtained in the middle sections of cavity ( $L=5$ ,  $Rm=1.8$ ). Comparison of SGM results with exp. data and SVV solutions of SÉVERAC *et al.* [5].

The shear stresses are smaller by one order than the main stress tensor components. Figure 14 presents examples of axial variations of the magnitude of shear stress vector in the plane parallel to the disks  $\sqrt{(v^{*'}w^{*'}^2 + u^{*'}w^{*'}^2)}$  and the magnitude of total shear stress vector  $(v^* \frac{\partial v^*}{\partial z^*} - v^{*'}w^{*'}, v^* \frac{\partial u^*}{\partial z^*} - u^{*'}w^{*'})$ , normalized by the total friction velocity  $v_\tau^*$ . We can see from Fig. 14 that after reaching maximum,  $\sqrt{(v^{*'}w^{*'}^2 + u^{*'}w^{*'}^2)}/v_\tau^{*2}$  decreases to the value charac-

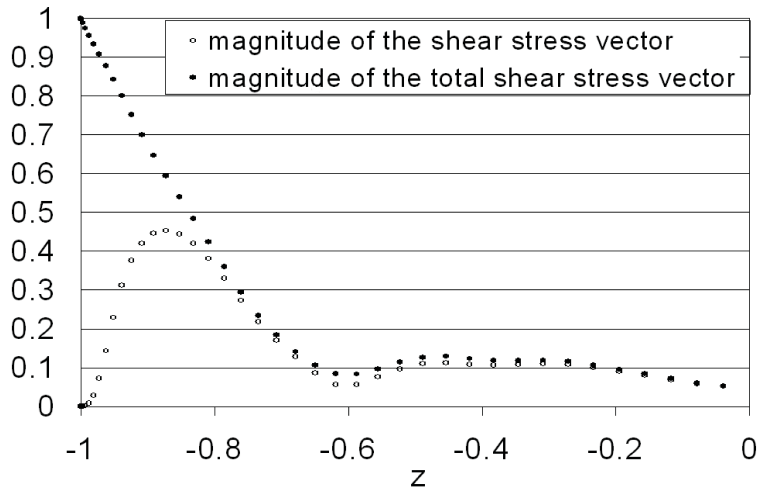


FIG. 14. The variations of the magnitude of the shear stress vector and magnitude of the total shear stress vector normalized by the total friction  $v_\tau^*$  velocity, ( $L = 5$ ,  $Rm = 3$ ,  $Re = 100000$ ,  $B = 0.1$ ,  $r = 0$ ). SGM.

teristic for the central core, whereas  $\left( \nu^* \frac{\partial v^*}{\partial z^*} - \overline{v^{*'} w^{*'}} , \nu^* \frac{\partial u^*}{\partial z^*} - \overline{u^{*' } w^{*'}} \right) / v_\tau^{*2}$  is constantly decreasing from its maximum value of 1.

## 8. Conclusions

The transitional flows in the sealed rotor/stator cavity have been investigated up to the Reynolds number 150000. The cavity was enclosed by the inner cylinder attached to the rotor and the outer one attached to the stator; the confinement effect was taken into account.

In the paper LES (with a high-order resolution method based on the spectral Chebyshev-Fourier approximation) of the transitional flow was performed. LES has been performed using the proposed SGM algorithm based on the version of dynamic Smagorinsky eddy viscosity model presented by MENEVEAU [41], in which the stabilizing averaging is performed over the fluid particle pathline. In this approach, the Smagorinsky coefficient at a given position of particle  $x$  depends on the history of the flow, which was ignored in the classical Smagorinsky approach. Averaging along the particle trajectories has a distinct advantage that it is applicable also to inhomogeneous flows. The SGM model allowed us to perform computations for higher Reynolds numbers in the rotating flows, which are strongly inhomogeneous and anisotropic due to the combined effects of rotation and confinement. MENEVEAU [1] approach was extended in the present research to the non-isothermal flow using the Boussinesq model.

To demonstrate effectiveness of the proposed algorithm and to verify it, computations were performed for the cavity of aspect ratio  $L = 5$  and curvature parameters  $Rm = 1.8$  and  $3.0$ , and for the Reynolds numbers up to  $150000$ . The structure of this kind of flows is highly complicated due to the existence simultaneously laminar, transitional and turbulent areas; the flow consists of two disjoint boundary layers on each disk, and of a central inviscid core. Additionally, the stator boundary layer is far more unstable than the rotor boundary layer. The axial mean velocity components profiles and the Reynolds stress tensor components profiles obtained for the cavity ( $L = 5$ ,  $Rm = 1.8$ ,  $B = 0$ ,  $Re = 100000$ ) were compared favorably with the experimental and SVV data of SÉVERAC *et al.* [5].

## Acknowledgments

The authors thank Prof. Patrick Bontoux from CNRS-Aix Marseille University and Prof. Akira Murata from Tokyo University for helpful consultations. The computations were carried out in the Poznan Supercomputing and Networking Centre, what is gratefully acknowledged. The work is supported by COST/78/2006.

## References

1. E. SÉVERAC, E. SERRE, *A spectral viscosity LES for the simulation of turbulent flows within rotating cavities*, J. Comp. Phys., **226**, 2, 1234–1255, 2007.
2. S. HUGUES, A. RANDRIAMAMPANINA, *An improved projection scheme applied to pseudospectral methods for the incompressible Navier-Stokes equations*, Int. J. Numer. Methods Fluids, **28**, 501, 1998.
3. I. RASPO, S. HUGUES, E. SERRE, A. RANDRIAMAMPANINA, P. BONTOUX, *Spectral projection methods for the simulation of complex three-dimensional rotating flows*, Computers and Fluids, **31**, 4–7, 745–767, 2002.
4. E. SERRE, J.P. PULICANI, *A three-dimensional pseudospectral method for rotating flows in a cylinder*, Computers & Fluids, **30**, 491, 2001.
5. E. SÉVERAC, S. PONCET, E. SERRE, *Large eddy simulations and measurements of turbulent enclosed rotor-stator flows*, Phys. Fluids, **19**, 085113, 2007.
6. S.P. WILKINSON, M.R. MALIK, *Stability experiments in the flow over a rotating disk*, AIAA J., **23**, 4, 588–595, 1985.
7. R. KOBAYASHI, Y. KOHAMA, M. KUROSAWA, *Boundary layer transition on a rotating cone in axial flow*, J. Fluid Mech., **127**, 341–352, 1983.
8. W.S. SARIC, H.L. REED, E.B. WHITE, *Stability and transition of three-dimensional boundary layer*, Annular Rev. Fluid Mech., **35**, 413–440, 2003.
9. H. LITTELL, J. EATON, *Turbulence characteristics of the boundary layer on a rotating disk*, J. Fluid Mech., **266**, 175–207, 1994.

10. H.S. KANG, H. CHOI, J.Y. YOO, *On the modification of the near-wall coherent structure in a three-dimensional turbulent boundary layer on a free rotating disk*, Phys. of Fluids, **10**, 2315, 1998.
11. E. TULISZKA-SZNITKO, C. SOONG, *Instability of non-isothermal flow between coaxial rotating disks*, Proceedings of European Congress on Computational Methods in Applied Sciences and Engineering, Barcelona 2000.
12. M. ITOH, *On the instability of the flow between coaxial rotating disks*, Boundary Layer Stability and Transition to Turbulence, ASME FED, **114**, 83, 1991.
13. A. RANDRIAMAMPINANINA, P. BONToux, B. ROUX, *Écoulements induits par la force gravifique dans une cavité cylindrique en rotation*, Int. J. Heat Mass Transf., **30**, 7, 1275–1292, 1987.
14. L. ELÉNA, R. SCHIESTEL, *Turbulence modeling of rotating confined flows*, Int. J. of Heat and Fluid Flow, **17**, 3, 283–289, 1996.
15. J.W. DAILY, R.E. NECE, *Chamber dimension effect on induced flow and friction resistance of enclosed rotating disk*, ASME J., Basic Eng., **82**, 217–232, 1960.
16. J.M. OWEN, R.H. ROGERS, *Heat transfer in rotating disc systems*, W.D. MORRIS [Ed.], Wiley, Taunton, Somerset, England, 1989.
17. J.M. OWEN, R.H. ROGERS, *Heat transfer in rotating disc systems*, W.D. MORRIS, Wiley, Taunton, Somerset, England, 1995.
18. L. SCHOUVEILER, P. LE GAL, P. CHAUVE, *Instabilities of the flow between a rotating and stationary disk*, J. Fluid Mech., **443**, 329–350, 2002.
19. G. GAUTHIER, P. GONDRET, F. MOISY, M. RABAUD, *Instabilities in the flow between co- and counter-rotating disks*, J. Fluid Mech., **473**, 1–21, 2002.
20. F. MOISY, O. DOARE, T. PASUTTO, O. DAUBE, M. RABAUD, *Experimental and numerical study of the shear layer instability between two counter-rotating disks*, J. Fluid Mech., **507**, 175–203, 2004.
21. S. PONCET, M. CHAUVE, R. SCHIESTEL, *Batchelor versus Stewartson flow structures in a rotor-stator cavity with throughflow*, Phys. Fluids, **17**, 075110, 2005.
22. S. CHEAH, H. IACOVIDES, D. JACKSON, H. JI, B. LAUNDER, *Experimental investigation of enclosed rotor-stator disk flows*, Exp. Therm. Fluid Sci., **9**, 45, 1994.
23. M. ITOH, Y. YAMADA, S. IMAO, M. GONDA, *Experiments on turbulent flow due to an enclosed rotating disk*, in Engineering Turbulence Modeling and Experiments, W. RODI and E. GANIC [Eds.], Elsevier, 659–668, 1990.
24. M. ITOH, Y. YAMADA, S. IMAO, M. GONDA, *Experiments on turbulent flow due to an enclosed rotating disk*, Exp. Term. Fluid, **9**, 445, 1994.
25. J. LOPEZ, J. HART, F. MARQUES, S. KITTELMAN, J. SHEN, *Instability and mode interactions in a differentially driven rotating cylinder*, J. Fluid Mech., **462**, 383–0409, 2002.
26. E. SERRE, E. CRESPO DEL ARCO, P. BONToux, *Annular and spiral patterns in flow between rotating and stationary disks*, J. Fluid Mech., **434**, 65–100, 2001.
27. E. SERRE, E. TULISZKA-SZNITKO, P. BONToux, *Coupled numerical and theoretical study of the transition flow between a rotating and stationary disk*, Phys. of Fluids, **16**, 3, 688–707, 2004.
28. J.J. HEALEY, *Enhancing the absolute instability of a boundary layer by adding a far-away plate*, J. Fluid. Mech., **579**, 29–61, 2000.

29. A. RANDRIAMAMPINANINA, L. ELÉNA, J.P. FONTAINE, R. SCHIESTEL, *Numerical prediction of laminar, transitional and turbulent flows in shrouded rotor-stator systems*, Physics of Fluids, **9**, 6, 1696–1713, 1997.
30. A. RANDRIAMAMPINANINA, S. PONCET, *Turbulence characteristics of the Bödewadat layer in a large enclosed rotor-stator system*, Phys. Fluids, **18**, 055104, 2006.
31. E. TULISZKA-SZNITKO, E. SERRE, P. BONToux, *On the nature of the boundary layers instabilities in a flow between a rotating and a stationary disc*, C.R. Mecanique, **30**, 90–99, 2002.
32. E. TULISZKA-SZNITKO, A. ZIELINSKI, *DNS/LES of transitional flow in rotating cavity*, Int. J. Transport Phenomena, **10**, 3, 223–234, 2008.
33. E. TULISZKA-SZNITKO, A. ZIELINSKI, W. MAJCHROWSKI, *LES and DNS of the non-isothermal transitional flow in rotating cavity*, accepted in Int. J. of Heat and Fluid Flow, 2009.
34. E. CRESPO DEL ARCO, P. MAUBERT, A. RANDRIAMAMPINANINA, P. BONToux, *Spatio-temporal behavior in a rotating annulus with a source sink flow*, J. Fluid Mech., **328**, 271–296, 1996.
35. O. CZARNY, H. IACOVIDES, B.E. LAUNDER, *Processing vortex structure in turbulent flow within rotor-stator disc cavities*, FTAC, **69**, 51–61, 2002.
36. M. LYGREN, H.I. ANDERSON, *Turbulent flow between a rotating and a stationary disk*, J. Fluid Mech., **426**, 297, 2001.
37. R. JACQUES, P. LE QUÉRÉ, O. DAUBE, *Axisymmetric numerical simulations of turbulent flow in rotor/stator enclosure*, Int. J. of Heat and Fluid Flow, **23**, 381–397, 2002.
38. X. WU, K.D. SQUIRES, *Prediction and investigation of the turbulent flow over a rotating disk*, J. Fluid Mech., **418**, 231–264, 2000.
39. H.I. ANDERSON, M. LYGREN, *LES of open rotor-stator flow*, Int. J. Heat Fluid Flow, **27**, 4, 551–557, 2006.
40. M. LYGREN, H.I. ANDERSON, *Large eddy simulations of the turbulent flow between a rotating and a stationary disk*, ZAMP, **55**, 268, 2004.
41. C. MENEVEAU, T.S. LUND, W.H. CABOT, *A Lagrangian dynamic subgrid-scale model of turbulence*, J. Fluid Mech., **319**, 353–385, 1996.
42. R. PASQUETTI, *Spectral vanishing viscosity method for large eddy simulation of turbulent flow*, J. Sci. Comp., **27**, 1–3, 365–375, 2006.
43. D. LILLY, *A proposed modification of the Germano subgrid-scale closure method*, Phys. Fluids A, **4**, 3, 633–635, 1992.
44. M. GERMANO, U. PIOMELLI, P. MOIN, W. CABOT, *A dynamic sub-grid eddy viscosity model*, Phys. of Fluids A, **3** (7), 1760–1765, 1991.
45. J.M. VANEL, R. PEYRET, P. BONToux, *A pseudospectral solution of vorticity-stream function equations using the influence matrix technique*, Num. Meth. Fluid Dyn., II, Clarendon, ed. Morton & Baines, 463–475, 1986.

Received 29 May, 2008; revised version 27 March, 2009.

---